3D normalized cross-correlation for estimation of the displacement field in ultrasound elastography

Morteza Mirzaei[a,*], Amir Asif[a], Maryse Fortin[b], Hassan Rivaz[a,b]

[a]Department of Electrical and Computer Engineering, Concordia University, Montreal, Quebec, Canada
[b]PERFORM Centre, Concordia University, Montreal, Quebec, Canada

Abstract

This paper introduces a novel technique to estimate tissue displacement in quasi-static elastography. A major challenge in elastography is estimation of displacement (also referred to time-delay estimation) between pre-compressed and post-compressed ultrasound data. Maximizing normalized cross correlation (NCC) of ultrasound radio-frequency (RF) data of the pre- and post-compressed images is a popular technique for strain estimation due to its simplicity and computational efficiency. Several papers have been published to increase the accuracy and quality of displacement estimation based on NCC. All of these methods use 2D spatial windows in RF data to estimate NCC, wherein displacement is assumed to be constant within each window. In this work, we extend this assumption along the third dimension. Two approaches are proposed to get third dimension. In the first approach, we use temporal domain to exploit neighboring samples in both spatial and temporal directions. Considering temporal information is important since traditional and ultrafast ultrasound machines are, respectively, capable of imaging at more than 30 frame per second (fps) and 1000 fps. Another approach is to use time-delayed pre-beam formed data (channel data) instead of RF data. In this method information of all channels that are recorded as pre-beam formed data of each RF line will be considered as 3rd dimension. We call these methods as spatial temporal normalized cross correlation (STNCC) and channel data normalized cross correlation (CNCC) and show that they substantially outperforms NCC using simulation, phantom and *in-vivo* experiments. Given substantial improvements of results in addition to the relative simplicity of implementing STNCC and CNCC, the proposed approaches can potentially have a large impact in both academic and commercial work on ultrasound elastography.

Keywords: Ultrasound Elastography, Quasi static Elastography, Time delay estimation, Normalized Cross Correlation (NCC), Spatial and Temporal Information, Channel data.

1. Introduction

Ultrasound imaging is one of the most commonly used imaging modalities since it is inexpensive, safe and convenient. Ultrasound elastography estimates biomechanical properties of the tissue and can substantially improve the capabilities of ultrasound imaging in both diagnosis and image-guided interventions. Elastography methods can reveal different mechanical properties such as viscosity or Poisson's ratio, but imaging elastic properties of the tissue is the most-widely used technique [1]. Elastography has been used in imaging breast [2, 3, 4, 5] and prostate cancer [6] as well as investigation of liver health [7, 8] and surgical treatment of liver cancer [9, 10, 11].

Estimation of tissue displacement due to an internal or external force is at the heart of all ultrasound elastography methods [12]. Elastography methods that are based on internal or endogenous deformation are often based on the pumping action of the heart which generates waves in the surrounding tissue. Mechanical properties of the cardiac tissue can be measured based on velocity of this wave [13, 14, 15]. In the case of external excitation, there are different techniques for exciting tissue and measuring its mechanical property but they can be broadly grouped into dynamic and quasi-static elastography. Dynamic methods such as shear wave imaging (SWI) [16, 17, 18] and acoustic radiation force imaging (ARFI) [19] can provide quantitative mechanical properties of tissue. Both SWI and ARFI use Acoustic Radiation Force (ARF) to generate displacement in the tissue.

Quasi-static elastography often generates the displacement in the tissue by simply pressing the probe against the tissue. The core idea of quasi-static approach that is also known as compression elastography is introduced in [20] but the concept of this technique is not a new one and estimation of tissue hardness by hand palpation is an ancient technique [21]. The main reason for name of quasi-static is that the velocity of deformation is very low such that static mechanics can be assumed [22]. This technique does not require additional hardware other than an ultrasound machine, and as such, is very convenient and has even been applied in image-guided surgery [23] and radiotherapy [24]. Compared to SWI and ARFI, displacements in quasi-static elastography are usually substantially larger, leading to a larger signal to noise ratio in displacement estimation. The disadvantage is that it cannot readily generate quantitative tis-

*Morteza Mirzaei, Department of Electrical and Computer Engineering, Concordia University, EV10.113, 1455 Maisonneuve west, Montreal, H3G 1M8; Email, m_irzae@ece.concordia.ca

sue properties and an inverse problem approach should also be applied to infer quantitative properties in tissue [25, 26, 27].

This paper entails estimation of tissue displacement, and as such, can be applied to almost all elastography methods. However, we focus on free-hand palpation quasi-static elastography, which involves slowly compressing the tissue with the ultrasound probe. Low cost and ease to availability are two advantages of free-hand palpation ultrasound elastography [28, 29]. In this method, the movement of the probe is largely in the axial direction and the main goal is to compute strain and deformation in the axial direction. However, even pure axial compression of probe will deform the tissue in all directions. Although axial deformation has most of useful elasticity information, lateral displacement can also be calculated [30, 31, 32, 33]. Estimation of out-of-plane deformation is currently not possible from two dimensional ultrasound images, and custommade probes [34] or three-dimensional ultrasound imaging is needed [23, 35, 36]. Deformation estimation is most accurate in the axial direction mainly due to lack of carrier for the lateral component of the reflected echo [37], smaller width of the point spread function in the axial direction [38] and also lower sampling frequency in the lateral direction [39].

Estimation of tissue displacement is often referred to as time delay estimation (TDE), which usually relies on raw radiofrequency (RF) data. Since one sample of RF data does not provide enough information to calculate displacement, most methods are based on dividing the RF data into several overlapping windows and calculating the displacement of each window [40, 41]. The underlying assumption here is that displacement of all samples within the window is the same, and therefore, additional information from the neighboring samples is exploited to calculate the displacement of the sample at the center of the window. This additional information helps reduce the estimation variance.

Maximization of the normalized cross correlation (NCC) of windows was one of the first approaches used for TDE, which is still a very popular approach because it is easy-to-implement and is computationally efficient [42, 43, 44]. Phase correlation wherein zero crossing of phase determines displacement [45, 46] and sum of absolute difference of windows [47] are other major window-based techniques for elastography.

Window-based techniques are easy to implement, but one of the most important disadvantages of these algorithms is false peaks. False peaks occur when a secondary NCC peak or zero crossing of phase or sum of absolute difference, exceeds true ones. False peaks are a common error in window-based elastography methods since all windows of post compressed image should be searched to find the best match. To overcome false peaks, time-domain cross correlation with prior estimates (TDPE) is introduced in [43]. In TPDE, only a small part of post compressed image should be searched for correlated window and the searching area is limited to a neighborhood around the previous time-delay estimate. By utilizing TDPE, the problem of false peaks can be addressed, but still window-based algorithms are sensitive to signal de-correlation which can be caused by the out of plane or lateral displacement which are common problems especially in free-hand palpation. Another
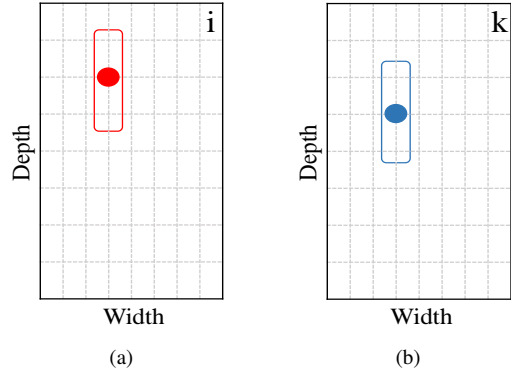

Figure 1: Two frames of ultrasound RF data corresponding to (a) pre- and (b) post-compression. Vertical dashed lines represent RF lines and intersection of vertical and horizontal lines represent RF samples. The images are severely down-sampled for visual illustration; a typical RF frame has many more samples. To find the displacement of the sample marked with a red circle, the red window around that sample is considered for calculating a similarity metric (usually NCC). The blue sample indicates the corresponding sample in the post-compression image.

major source for signal de-correlation is blood flow and other biological motions that are common in *in-vivo* data.

In all of the aforementioned studies, the RF lines of just two images are compared with each other and the displacement fields across small spatial windows are assumed to be constant as it is shown in Fig.1.

In this paper we propose to utilize 3D information instead of 2D data and for the third dimension we have two options. In the first method, inspired by [48], we extend 2D spatial information to the temporal domain. We consider the cine ultrasound RF data as three-dimensional, where the third dimension is the time domain. In other words, based on high frame rate of ultrasound machine, we consider a set of temporally neighboring frames as pre-compressed data and a set of temporally neighboring frames as post-compressed data as shown in Fig.2. In the second approach, we consider time-delayed pre-beam-
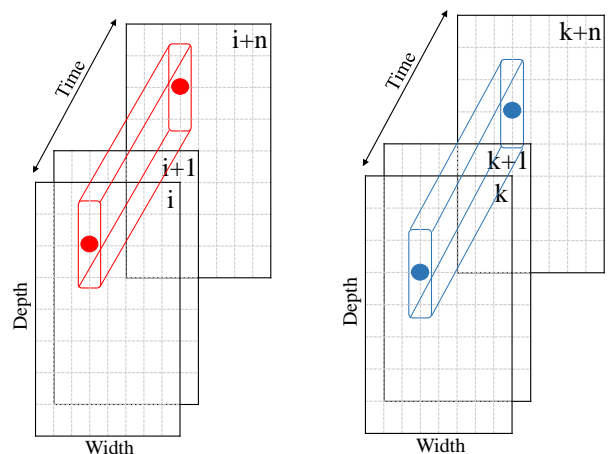

Figure 2: Two sequence of data used for spatial and temporal estimation of normalized correlation. The similarity metric (NCC in this work) is computed using the data in the 3D red and blue boxes.

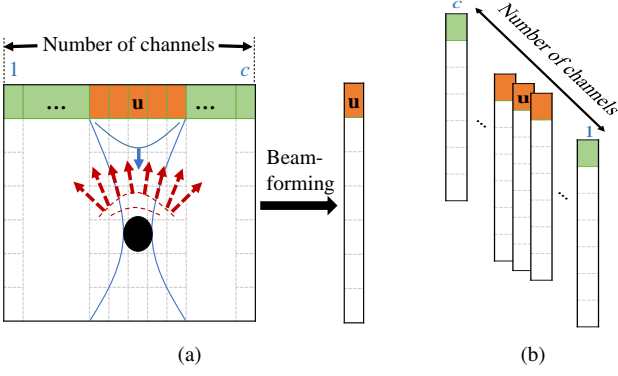formed data (channel data) for ultrasound elastography. In ul-

Figure 3: All of received data (shown in red dashed-arrows) will be beamformed to generate one line corresponding to 'u'(a). We rearrange time-delayed information of neighboring elements as shown in (b) to utilize them for CNCC.

trasound imaging, for generating an RF line several crystals record reflected waves. Time gain and also time delay due to transmission will be compensated and all data will be summed up to make one RF line. In this work we propose to use time gain and also time delay compensated channel data instead of RF data for elastography, where in for each RF line its corresponding channels will be considered as third dimension as it is shown in Fig.3.

We maximize NCC in between three-dimensional windows, and therefore, we name our first proposed algorithms as spatial temporal normalized cross correlation (STNCC) and the second one as channel data normalized cross correlation (CNCC). These simple and intuitive ideas substantially improves results of TDE. It is important to note that although the windows that we utilize to calculate NCC are three-dimensional, the estimated displacement field is two-dimensional.

STNCC and CNCC are more robust to signal de-correlation compared to NCC as shown in the simulation experiments. We also show that as the amplitude of noise increases, STNCC exhibits much less susceptibility as compared to NCC. In addition, STNCC and CNCC are less sensitive to the window size in comparison to NCC. The codes of STNCC and CNCC will be made publicly available in https://users.encs.concordia.ca/ hrivaz/Ultrasound_Elastography/ after acceptance of this paper.

This paper is organized as follows: The STNCC and CNCC methods are presented in the Section 2. Simulation, phantom and *in-vivo* experiments using data obtained from back muscle and liver are studied in the Section 3. The results of the STNCC and CNCC methods are compared against traditional NCC. Discussions of the results and avenues for future work are presented in the Section 4, and the paper is concluded in the Section 5.

2. Methods and Materials

2.1. STNCC and CNCC for Elastography

Most elastography methods consider two images I_1 and I_2 as pre- and post-compressed images and calculate displacement of tissue using RF data of these images. The pre-compressed RF data set is divided into several windows and for each window one should look for a window in the post compressed RF data set that maximizes NCC as shown in Fig. 1.

NCC for two windows A and B is calculated as

$$NCC(A, B) = \frac{\sum_{j=1}^{j=W} A(j)B(j)}{\sqrt{\sum_{j=1}^{j=W} A(j)^2 \sum_{j=1}^{j=W} B(j)^2}}, \quad (1)$$

where W is the number of samples in the windows and j represents samples of windows. The peak of NCC corresponds to the displacement of windows in the pre-compressed image. Maximization of NCC only provides an integer displacement estimate, and interpolation should be performed to find a more accurate sub-pixel displacement estimate [49, 32, 50].

In this paper two novel techniques are introduced to use temporal or channels information. Hence instead of two 2D windows, two three-dimensional boxes should be considered as shown in Figs. 2 and 3. In these techniques, one should look for a box in the second sequence that has the maximum NCC with the box of first sequence and peak of NCC represents displacement of the center of first box. The only assumption of these algorithms is that all samples within the box have equal displacements. This is a good assumption for STNCC since the frame rate of ultrasound machines are more than 30 fps (more than 500 fps if plane-wave imaging is used) and consecutive frames (the third dimension of data for STNCC) and their displacement will be very close to each other. It is also worthwhile to mention that by considering temporal neighbors for STNCC, temporal behavior of the estimated strains improves significantly. Temporal accuracy plays an important role in poroelastic elastography [51], viscoelasticity measurment of the tissue [52], dynamic elastography methods such as shear-wave elastography [53, 54] and vibro-elastography [55]. The results of temporal behavior of the estimated strains by STNCC are reported in the supplementary material. For CNCC the assumption of same displacement for all samples of a box is exactly same as assumption that was made for 2D Rf data.

By considering the third dimension of size n for each box, the NCC of the two boxes is defined as

$$NCC(A, B) = \frac{\sum_{l=1}^{l=n} \sum_{j=1}^{j=W} A_l(j)B_l(j)}{\sqrt{\sum_{l=1}^{l=n} \sum_{j=1}^{j=W} A_l(j)^2 \sum_{l=1}^{l=n} \sum_{j=1}^{j=W} B_l(j)^2}} \quad (2)$$

where A_l and B_l are windows in the lth layer of the third dimension for the first and second boxes. W is the number of samples in a 2D window and j shows samples of 2D windows. The peak of STNCC or CNCC provides an integer displacement estimate and has to be interpolated to generate a subpixel displacement estimation. To avoid false peaks and to reduce the computational complexity of the algorithm, the search area is determined based on the displacement of the neighboring boxes. By calculating the displacement field, strain of the tissue can be determined by differentiating displacement field in the axial direction. Differentiating amplifies the noise, and therefore, least square techniques are common method to obtain the strain field.

2.2. Data Acquisition

In this section we describe the data that is utilized in different experiments of the paper and then results of STNCC and CNCC are provided in the Results Section and compared with NCC in two separate subsections. For sake of comparison, Signal to noise ratio (SNR) and contrast to noise ratio (CNR) are used to provide quantitative means for assessing the proposed method according to

$$\text{SNR} = 10log_{10}(\frac{\bar{s}}{\sigma}), \quad \text{CNR} = 10log_{10}\Big(\sqrt{\frac{2(\bar{s}_b - \bar{s}_t)^2}{\sigma_b^2 + \sigma_t^2}}\Big), \quad (3)$$

where $\bar{s}_t$ and $\bar{s}_b$ are the spatial strain average of the target and background, σ_b^2 and σ_t^2 are the spatial strain variance of the target and background, and $\bar{s}$ and σ are the spatial average and standard deviation of an arbitrary window in the strain image, respectively.

In all simulations and experiments, 7 frames are considered for STNCC and outputs of STNCC are compared with strains of middle frames that are estimated by NCC.

In all experiments (except the back muscle experiment) windows of size 10λ where λ is wavelength with 86% overlap of windows are considered and 3-point parabolic interpolation is utilized to find the 2D sub-sample location of the correlation peak. For the back muscle experiment, overlap of windows is reduced to 70% and 30% to show its effect on STNCC and NCC.

Simulation Data

A simulated phantom is generated by utilizing the Field II ultrasound simulation software [56]. FEM-based deformations are computed using the ABAQUS software package (Johnston, RI, USA). The simulated phantom is homogeneous except for a cylindrical inclusion with zero stiffness which is placed in the middle of phantom as an inclusion. The ground truth strain is shown in Fig. 4 where the white part represents the inclusion. The inclusion simulates a blood vein that easily compresses under force. Zero stiffness can be obtained by considering a hole inside the phantom. It will not lead to infinite strain because the surrounding medium supports the hole from collapsing. The Young module of background is equal to $4kPa$ in our simulation.

To make simulation experiment more realistic, images are normalized and uniform noises are added to images as

$$I_{ij} = \frac{I_{ij}}{\max_{i,j}(I_{ij})} + \text{noise}. \quad (4)$$

For calculating signal to noise ratio and contrast to noise ratio, for each level of noise we ran a Monte Carlo simulation by estimating strain 100 times with different random noise. The SNR of the noisy data is calculated as

$$\text{SNR} = 10log_{10}\Big(\frac{\text{mean}\big(I_{ij}^2\big)}{\text{mean}\big(\text{noise}^2\big)}\Big). \quad (5)$$
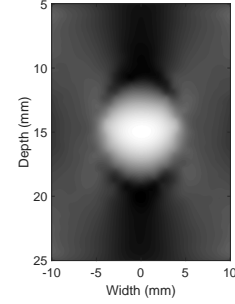

Figure 4: Ground truth strain in the simulation phantom. The displacement is estimated using the ABAQUS FEM software.

Phantom Data

We use conventional beam-formed, plane wave RF data and time-delayed channel data for comparison of STNCC and CNCC with NCC. Conventional beam-formed RF data is acquired from a tissue mimicking breast phantom (CIRS, Norfolk, VA, USA) with an Antares Siemens ultrasound machine (Siemens, Issaquah, WA, USA) and VF 13-5 probe at the center frequency of 7.27 MHz, sampling frequency of 40 MHz and frame rate of 37 fps.

Plane wave RF data and also channel data are acquired from a tissue mimicking phantom (059 tissue mimicking breast phantom, CIRS tissue simulation & phantom technology, Norfolk, VA, USA) using an E-Cube R12 ultrasound machine (Alpinion, Bothell, WA, USA) with a L3-12H probe at the center frequency of 11.5 MHz, sampling frequency of 40 MHz. It should be mentioned that plane wave are collected at frame rate of 504 fps.

in-vivo Data

Two different *in-vivo* RF data sets are utilized for comparing STNCC and NCC. The first data set is back muscle that *in-vivo* RF data are collected using an E-Cube R12 ultrasound machine (Alpinion, Bothell, WA, USA) with a SC1-4H curvilinear probe at the center frequency of 3.2 MHz and sampling frequency of 40 MHz at Concordia University. This study was approved by Central Ethics Committee of Health and Social Services from the Ministry of Quebec (MSSS: Ministere de la Sante et des Services Sociaux). The subject provided informed consent for participating in this study. The probe was hand-held and was placed axially on the lower back multifidus muscle while the subject was lying prone. The subject then performed a contra lateral arm lift, which causes deformation (sub-maximal contraction) in the multifidus muscle. Fig. 10 (a) shows B-Mode image of the multifidus muscle, which is delineated by dashed red lines.

The second data set is liver data that is acquired from a patient undergoing open surgical radio frequency thermal ablation for liver cancer before ablation. This data was collected at the Johns Hopkins hospital with an Antares ultrasound machine (Siemens, Issaquah, WA, USA) with a VF10-5 linear probe with a center frequency of 6.6 MHz, sampling frequency of 40 MHz and frame rate of 30 fps. The study was approved by the ethics institutional review board at Johns Hopkins. Fig. 11 (a)

shows the B-Mode image, where the tumor is marked with red arrows.

(a)　　　　(b)　　　　(c)
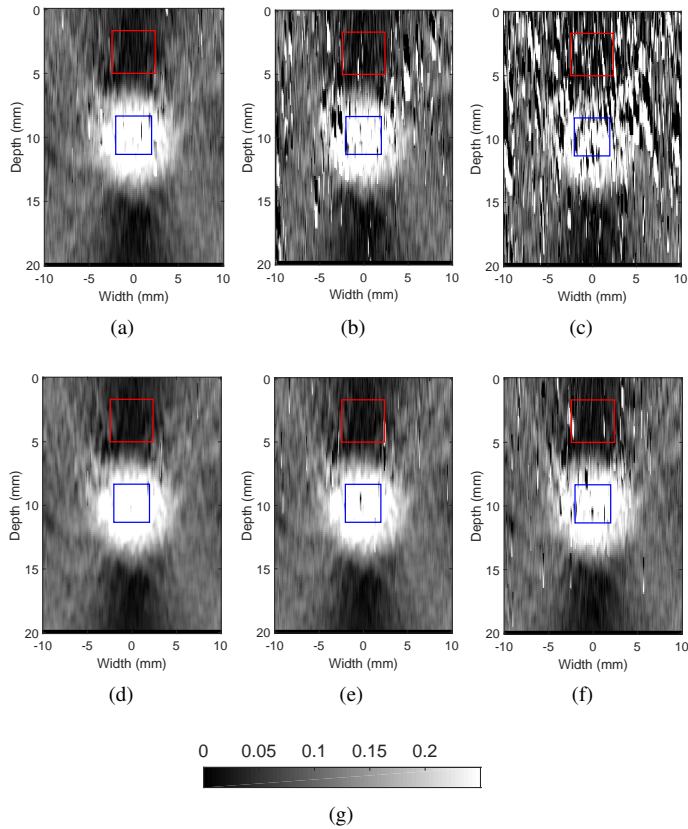
(d)　　　　(e)　　　　(f)

0　0.05　0.1　0.15　0.2

(g)

Figure 5: Strain images of the simulation phantom calculated using NCC and STNCC. The first row shows strain images that are calculated using NCC, and the second row depicts strain images computed using STNCC. In the first, second and third columns, the SNR values of data are 6.55 dB, 3.56 dB and 2.17 dB, respectively.

3. Results

3.1. STNCC

In this part, results of the proposed STNCC method are presented and compared against NCC for simulated phantom and experimental data in separate subsections.

3.1.1. Simulation Results

The phantom is compressed by 0.5% and the compression rate between two consecutive frames is 0.02%. To make simulation experiment more realistic, noises are added to images in three steps with zero mean and standard deviation of 0.086, 0.144 and 0.202. Fig. 5 shows outputs of STNCC and NCC for different levels of noise. It is clear that results of STNCC are closer to ground truth and outperform results of NCC. Higher signal to noise ratio and contrast to noise ratio of STNCC that are represented in Table 1 also validate better performance of STNCC. For each level of noise we ran a Monte Carlo simulation by estimating strain 100 times with different random noise.

Table 1: The mean and variance of SNR and CNR for 100 strain images of the simulated phantom for different methods and noise levels. Windows that are considered for calculating CNR are shown in blue and red lines in Figure 5. The red window is considered for SNR.

SNR of noisy data mean (var.)		SNR mean (var.)	CNR mean (var.)
6.55	STNCC	1.56 (0.16)	7.07 (0.40)
	NCC	0.26 (1.32)	5.49 (0.82)
(6.91×10^{-5})	**Improvement**	**22.91%**	**43.87%**
3.56	STNCC	0.86 (0.86)	6.22 (0.56)
	NCC	-4.18 (2.86)	2.46 (1.45)
(8.14×10^{-5})	**Improvement**	**219.15%**	**137.68%**
2.17	STNCC	-1.17 (2.66)	4.64 (1.12)
	NCC	-10.59 (23.32)	-1.03 (4.24)
(7.53×10^{-5})	**Improvement**	**774.98%**	**268.97%**

The mean and variance of SNR and CNR for these 100 experiments are reported at Table 1.

As one can see in Fig. 5 and Table 2 not only STNCC outperforms NCC for each range of noise, but also has more robust performance against increasing the amplitude of noise.

Table 2: Effect of increasing noise on SNR and CNR values.

SNR of noisy data	Method	SNR%	CNR%
From 6.55 to 3.56	STNCC	-14.88	-17.77
	NCC	-64.02	-50.22
From 3.56 to 2.17	STNCC	-37.33	-30.49
	NCC	-77.14	-55.22

In the next experiment, we compressed the simulated phantom by 1%, 1.5% and 2% and repeated the experiment for these amount of compression. For representing CNR, simulation is run 100 times for each case and it is shown in Fig. 7 that for all three compression rate and for all three different noise levels, STNCC has better performance than NCC.

3.1.2. Conventional Beamforming Phantom Results

Similar to the previous section, the images are normalized and uniform noises are added to images in three steps with zero mean and standard deviation of 0.028, 0.144 and 0.202. The estimated strains obtained from STNCC and NCC are shown in Fig. 6.

As one can see, results of STNCC outperform NCC. Also, STNCC is more robust to increasing magnitude of noise. For computing SNR and CNR for each level of noise, experiments are repeated for 100 times and mean and variance of SNR and CNR are presented in Table 3. Edge spread functions of strains obtained by NCC and STNCC are shown in Fig. 8. For calculating edge spread function, two rectangular with length of 60 and width of 10 pixels are considered in strain of NCC and STNCC as shown in Figure 8 (a). The edge spread function is calculated by averaging intensity of pixels across width of these

(a) (b) (c)
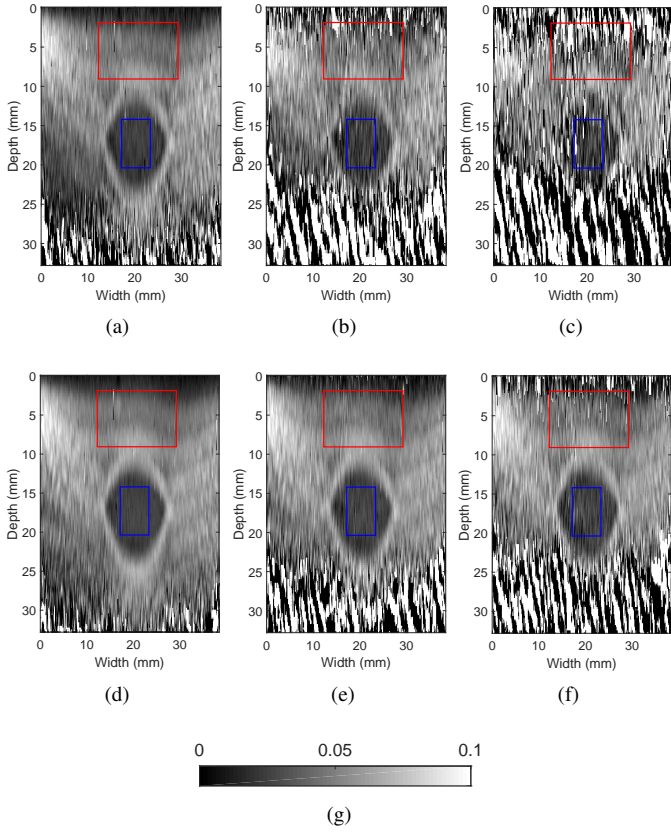
(d) (e) (f)

0   0.05   0.1

(g)

Figure 6: Comparison of strains that are calculated using NCC and STNCC for phantom data. The first and second rows show strain images calculated using NCC and STNCC, respectively. In the first, second and third columns, the SNR of data are 13.95 dB, 5.62 dB and 2.91 dB, respectively.
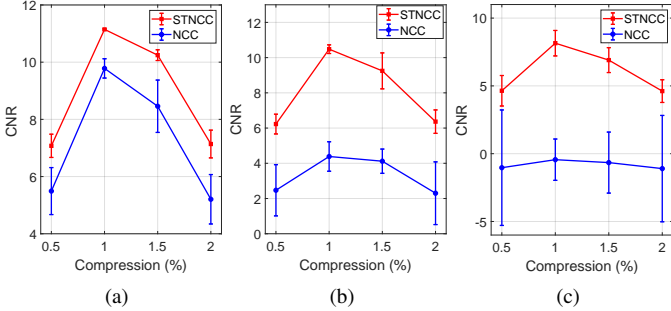

(a) (b) (c)

Figure 7: CNR values for different levels of compression and noise. The SNR of data in (a), (b) and (c) are respectively 6.55 dB, 3.56 dB and 2.17 dB.

rectangular and it is clear in Figure 8 (b) that the edge spread function of STNCC is smoother than NCC.

3.1.3. Plane wave imaging

As was explained in the Simulation Section, images are normalized and three different uniformly distributed noises with zero mean and standard deviation of 0.014, 0.043 and 0.072 are applied to images. The first and second rows of Fig. 9 show strain fields that are estimated by normal NCC and the proposed STNCC method, respectively. In the first, second and third columns the SNR values of data are 19.63 dB, 10.45 dB

Table 3: Mean and variance of SNR and CNR in 100 strain images for the conventionally beam-formed RF data of the phantom at different noise levels. Windows that are considered for calculating SNR and CNR are shown in Figure 6 (SNR is computed in the red windows only).

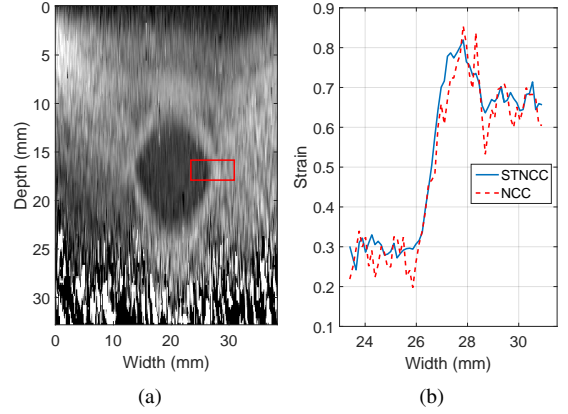| SNR of noisy data mean (var.)		SNR mean (var.)	CNR mean (var.)
13.95	STNCC	2.53 (0.07)	6.16 (0.07)
	NCC	2.09 (0.14)	5.37 (0.12)
(4.04×10^{-5})	**Improvement**	**21.05**%	**14.17**%
5.62	STNCC	1.33 (0.57)	4.86 (0.41)
	NCC	-7.08 (0.86)	-3.27 (0.52)
(3.81×10^{-5})	**Improvement**	**118.78**%	**248.62**%
2.91	STNCC	-6.21 (0.68)	-2.12 (0.5)
	NCC	-9.79 (0.7)	-6.20 (0.53)
(4.17×10^{-5})	**Improvement**	**128.03**%	**155.85**%

(a) (b)

Figure 8: Edge spread function for strain images that are calculated using NCC and STNCC. The red box in (a) shows the region of strain image where edge profiles are plotted. (b) shows the edge profiles.

and 6.66 dB, respectively. In all cases, the proposed method has a substantially better performance than normal NCC. Table 4 represents better performance of STNCC more explicitly.

3.1.4. Back Muscle Data

Fig. 10 (b), (d) show the displacement fields estimated with NCC and STNCC with 70% overlap between windows. Fig. 10 and Table 5 demonstrate that STNCC calculates a superior displacement field compared to NCC. We performed another comparison by changing the overlap between consecutive windows. Fig. 10 (c), (e) show the displacement field estimated with STNCC and NCC with 30% overlap of windows. Comparing Fig. 10 (b), (d) and 10 (c), (e), and also considering Table 5, it is clear that STNCC is substantially less susceptible to overlap between windows.

3.1.5. Liver Data

The estimated strains are presented in Figure 11 (b)-(c). Visual comparison of the strain images shows that STNCC generates a strain image with less noise. This is corroborated with
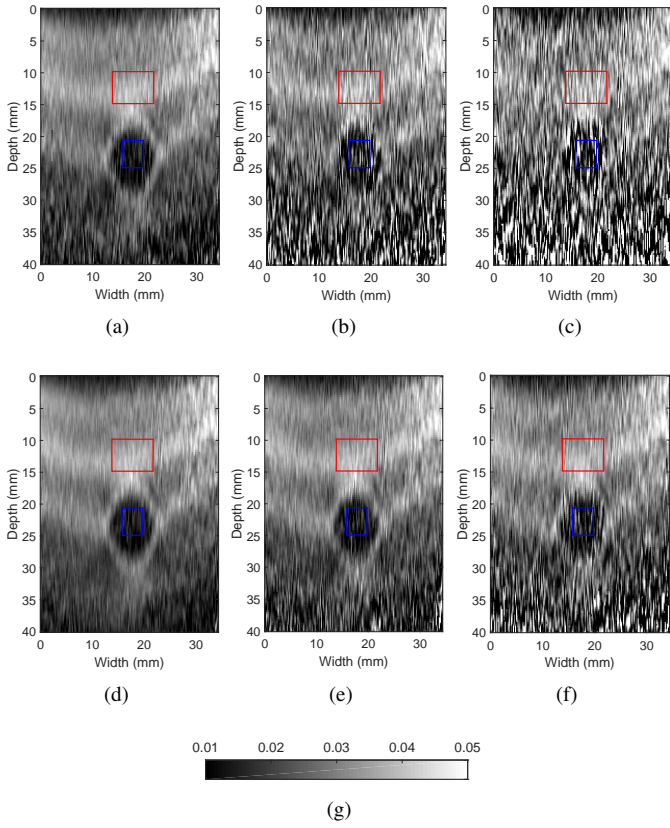
Figure 9: Comparison of strains that are calculated using NCC and STNCC for plane wave phantom data. The first and second rows show strain images calculated using NCC and STNCC, respectively. In the first, second and third columns, SNR values of data are 19.63 dB, 10.45 dB and 6.66 dB, respectively.

quantitative results of Table 6, which shows SNR and CNR. Compared to NCC, STNCSS improves SNR and CNR by respectively 52.4% and 67.49%.

Table 4: The mean and variance values of SNR and CNR in 100 strain images of the Plane wave data of phantom with different noise levels. Windows that are considered for calculating SNR and CNR are shown in Figure 9 (SNR is computed in the red windows only).

SNR of noisy data mean (var.)		SNR mean (var.)	CNR mean (var.)
19.63	STNCC	9.89 (0.002)	11.63 (0.01)
	NCC	9.72 (0.01)	10.71 (0.05)
(4.61×10^{-5})	**Improvement**	**1.74%**	**8.59%**
10.45	STNCC	9.63 (0.01)	10.18 (0.09)
	NCC	8.42 (0.05)	7.22 (0.1)
(5.2×10^{-5})	**Improvement**	**14.37%**	**40.99%**
6.66	STNCC	9.15 (0.03)	8.22 (0.2)
	NCC	6.90 (0.07)	3.91 (1.41)
(6.33×10^{-5})	**Improvement**	**67.88%**	**169.77%**

Table 5: SNR of displacement images of the back muscle. The black window is considered in calculating SNR.

Overlap of windows		SNR
	STNCC	-0.89
70%	NCC	-2
	Improvement	**29.12%**
	STNCC	-1.0
30%	NCC	-2.88
	Improvement	**54.17%**

3.2. CNCC

3.2.1. Simulation Results

The phantom is compressed by 1% and time-delayed channel data is acquired from Filed II software for CNCC experiment. Same channel data are summed-up to generate corresponding RF data. Strain fields estimated by NCC and CNCC are illustrated in Fig. 12. To further clarify better performance of

Table 6: SNR and CNR values in strain images of Figure 11. Windows that are considered for calculating CNR are shown in Figure 11 and only red window is considered for SNR.

	SNR	CNR
STNCC	4.31	5.39
NCC	2.48	3.15
Improvement	**52.4%**	**67.49%**

CNCC, a histogram analysis is done for CNR and SNR comparison in Fig. 13. We have moved the small blue colored window within the big blue window to take 12 target windows. At the same time, the small red colored window is swiped within the large red window to consider 32 background windows. CNR is calculated for every combination of target and background windows and SNR is calculated for all 32 background windows. It is clear that for small SNR and CNR values, NCC has higher frequencies than CNCC but for higher values of SNR and CNR, CNCC has higher frequency.

3.2.2. Phantom Results

For fair comparison of CNCC and NCC, channel data that are utilized for providing results of CNCC are beam-formed with the same ultrasound machine and then feed to NCC. Estimated strains of CNCC and normal NCC are shown in Fig. 14. For comprehensive CNR and SNR comparison, histogram analysis is done which is shown in Fig. 15. We have moved the small red colored window within the big red window to take 12 target windows. At the same time, the small blue colored window is swiped within the large blue window to consider 24 background windows. CNR is calculated for every combination of target and background windows and SNR is calculated for all 24 background windows. Fig. 15 shows distribution of the aforementioned 288 CNR values and 24 SNR values. It is clear that for small SNR and CNR values, NCC has higher frequencies than CNCC but for higher values of SNR and CNR, CNCC has higher frequency.
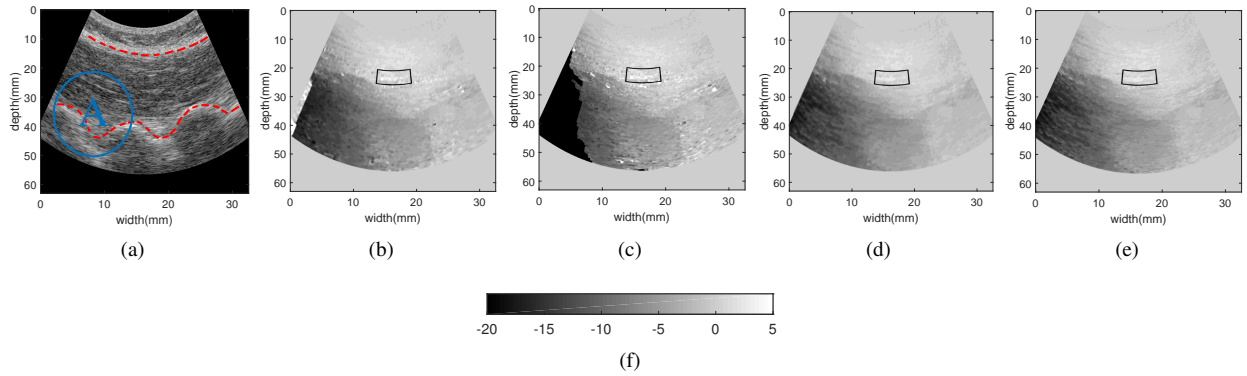
Figure 10: B-mode image of the back muscle (a). Red dashed lines delineate the multifidus muscle. Visual inspection of the B-mode images shows the maximum displacement occurring in the region marked with the letter A. Displacement fields of the back muscle calculated using NCC (b)-(c) and STNCC (d)-(e). The overlap between windows are 70% (b), (d) and 30% (c), (e).
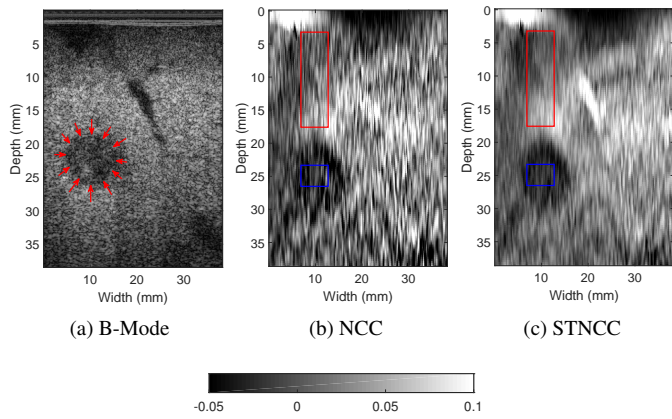

Figure 11: B-mode image of the liver with a tumor (marked with red arrows). Strain images calculated using NCC and STNCC are shown in (b) and (c) respectively.
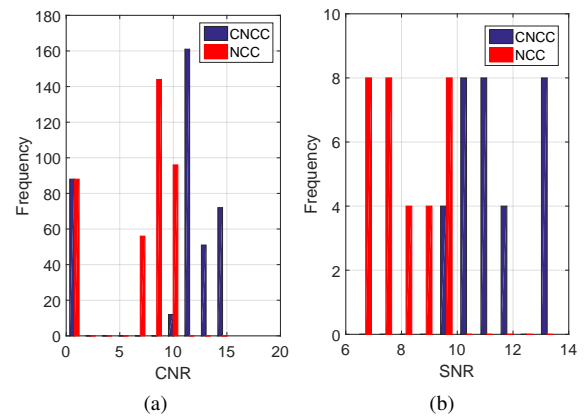

Figure 13: histogram distribution of CNR (a) and SNR (b) for estimated strain of simulated phantom by NCC and CNCC.
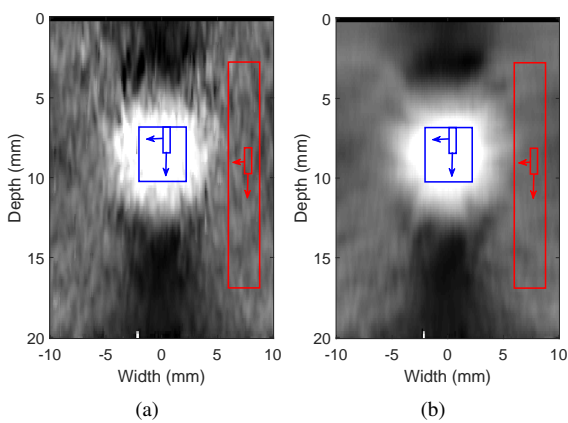

Figure 12: Strain images of simulated phantom calculated using NCC and CNCC are shown in (a) and (b) respectively.
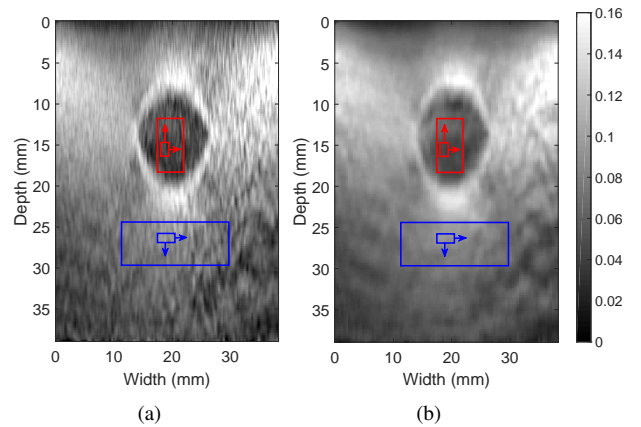

Figure 14: Strain images of experimental phantom calculated using NCC and CNCC are shown in (a) and (b) respectively.

4. Discussion

One of the most challenging issues in most of computer vision techniques such as optical flow computation is dealing with ill-posed problems. Each sample that moves in 3D dimension (axial, lateral and out of plane) has three unknowns to be tracked, however intensity equality of one sample in the two images provides only one equation. Window-based track-
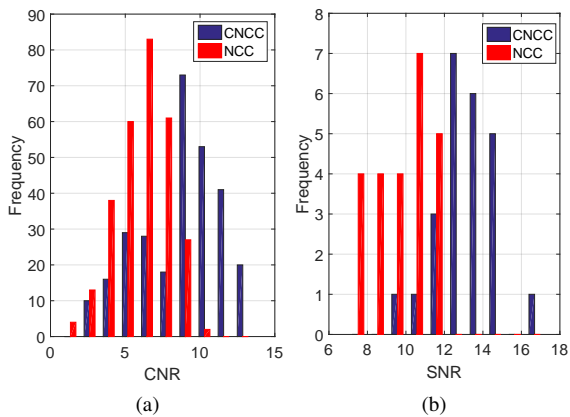
Figure 15: Histogram distribution of CNR (a) and SNR (b) for estimated strain of experimental phantom by NCC and CNCC.

ing methods are one of the most popular techniques to make tracking a well-posed problem. These techniques assume that displacements of spatially neighboring samples are the same and look for a similar window in the other image. According to detailed experiments in [57, 58], assuming that λ is one wavelength of ultrasound signal, 10λ is approximately largest window size for which this assumption is valid. The underlying idea of this project was extending the assumption of spatial continuity to temporal continuity or using channel data instead of RF data.

In traditional window-based methods, 2D spatial windows were considered and information of spatially neighbors was utilized. In this paper, we use 3D window to benefit from additional information made available by including samples in the third dimension. In this paper, two approaches named by STNCC and CNCC are proposed. In STNCC, the third dimension is temporally neighboring samples. The idea of considering temporal neighbors to estimate displacement makes sense by noting that traditional and ultrafast ultrasound machine has capability of imaging more than 30 and 1000 frame per seconds. Therefore, displacement between consecutive frames will be very small which allows the well-known spatial assumption of window based methods to be extended to the temporal domain. In CNCC as the second proposed method for utilization of 3D information, time-delayed pre-beam-formed data that is collected by neighboring channels are utilized as the third dimension. In all previously proposed methods, B-mode or RF data was used for elastography; however we know that for generating one RF line, several neighbor channels collect data and after applying appropriate time-delay, they sum up to generate one RF line. Therefore each RF sample results form summation of several channel samples. The underlying idea of CNCC is that comparing all components that make a RF sample will lead to more accurate displacement estimation than comparing two individual RF samples.

To illustrate better performance of proposed methods, different experimental set-ups are used. A simulated phantom with an soft inclusion is made by Field II package and is deformed by the finite element ABAQUS software. The reason we per-

form this simulation is to illustrate the performance of the proposed algorithms with both hard (e.g. phantom and in-vivo) and soft inclusions. In the next experiment different tumors of a tissue mimicking breast phantom is imaged in different modalities (Conventional beam-forming, plane wave and channel data) to show in-dependency of the proposed method to collected data. Finally, *in-vivo* results are presented to further clarify better performance of the proposed methods.

It is also shown that STNCC and CNCC are more robust to signal de-correlation and can tolerate higher levels of noise compared to NCC. A reason for this improvement is that noise affects different frames or channels at different levels, and by considering multiple frames or channels instead of one, the samples that are less noisy can compensate for the effect of noisy samples. A comment raised about STNCC, is estimating strain fields between different frames individually and averaging them to reduce the noise effect. This idea is helpful for large number of frames. However in STNCC, a small number of neighboring frames are considered to estimate displacement more accurately. The second reason for superiority of STNCC to averaging is computation cost. STNCC is much more effective than computing NCC for each pair individually and averaging them. For the simulated data of size 1041×250, NCC method takes 4.04 seconds for each pair of frames on a 3.20 GHz i7 Intel CPU. Therefore for estimating 7 strain fields and averaging them we need 28.285 seconds, however, STNCC takes only 9.70 seconds. The codes of STNCC and CNCC will be made publicly available in https://users.encs.concordia.ca/ hrivaz/Ultrasound_Elastography/ after acceptance of this paper.

Another advantage of these ideas pertains to a wealth of previous work on improving displacement estimation techniques with window-based methods. Future work can focus on applying those methods to 3D windows to further improve the performance of elastography methods.

Finally, estimated axial displacement are differentiated to get the axial strain field. For differentiation of each sample, a window of size $(2k + 1) \times 1$ has been considered around the reference sample. Utilizing the least square method, a line is fitted to these samples and its slope is regarded as the strain value of that sample. Moving the center of the window forward by one sample the strain of the next sample is calculated. It is clear that a large value for k makes the image smoother at the cost of losing information, while a small k may increase noise in strain estimation. We have used windows of length 17 (i.e. $k = 8$) for simulation, phantom and *in-vivo* results.

5. Conclusions

Ultrasound systems are capable of acquiring images at a very high frame rate. This capability is not exploited in previous window-based elastography algorithms where the windows were only in the spatial domain. Besides of high frame rate, we know that for generating one RF line multiple channels are employed to record data and RF line is beam formed of them. In this paper, a novel idea was proposed to consider third dimension of information which can be two sequence of images

instead of just two images or considering all channels that play role in producing one RF line. In these methods, 3D boxes in the first series are matched to those of the second series. It was shown using simulation, phantom and *in-vivo* experiments that extension of information to third direction substantially improves the quality of displacement estimation.

Acknowledgments

References

[1] T. L. Szabo, Diagnostic ultrasound imaging: Inside out, in: Academic Press, 2014.

[2] B. S. Garra, E. I. Cespedes, J. Ophir, S. R. Spratt, R. A. Zuurbier, C. M. Magnant, M. F. Pennanen, Elastography of breast lesions: initial clinical results., Radiology 202 (1) (1997) 79–86.

[3] T. J. Hall, Y. Zhu, C. S. Spalding, In vivo real-time freehand palpation imaging, Ultrasound in Medicine & Biology 29 (3) (2003) 427 – 435.

[4] M. Doyley, J. Bamber, F. Fuechsel, N. Bush, A freehand elastographic imaging approach for clinical breast imaging: system development and performance evaluation, Ultrasound in Medicine and Biology. 27 (10) (2001) 1347–1357.

[5] N. Uniyal, H. Eskandari, P. Abolmaesumi, S. Sojoudi, P. Gordon, L. Warren, R. N. Rohling, S. E. Salcudean, M. Moradi, Ultrasound rf time series for classification of breast lesions, IEEE Transactions on Medical Imaging 34 (2) (2015) 652–661.

[6] A. Lorenz, H. J. Sommerfeld, M. Garcia-Schurmann, S. Philippou, T. Senge, H. Ermert, A new system for the acquisition of ultrasonic multicompression strain images of the human prostate in vivo, IEEE Transactions on Ultrasonics, Ferroelectrics, and Frequency Control 46 (5) (1999) 1147–1154.

[7] T. Qiu, H. Wang, J. Song, G. Guo, Y. Shi, Y. Luo, J. Liu, Could ultrasound elastography reflect liver function?, Ultrasound in Medicine & BiologyIn press.

[8] Y. Chen, Y. Luo, W. Huang, D. Hu, R. qin Zheng, S. zhen Cong, F. kun Meng, H. Yang, H. jun Lin, Y. Sun, X. yan Wang, T. Wu, J. Ren, S.-F. Pei, Y. Zheng, Y. He, Y. Hu, N. Yang, H. Yan, Machine-learning-based classification of real-time tissue elastography for hepatic fibrosis in patients with chronic hepatitis b, Computers in Biology and Medicine 89 (2017) 18 – 23.

[9] H. Rivaz, E. M. Boctor, M. A. Choti, G. D. Hager, Ultrasound elastography using multiple images, Medical Image Analysis 18 (2) (2014) 314 – 329.

[10] W. Yang, T. J. Ziemlewicz, T. Varghese, M. L. Alexander, N. Rubert, A. N. Ingle, M. G. Lubner, J. L. Hinshaw, S. A. Wells, F. T. Lee Jr, et al., Post-procedure evaluation of microwave ablations of hepatocellular carcinomas using electrode displacement elastography, Ultrasound in medicine & biology 42 (12) (2016) 2893–2902.

[11] N. Frulio, H. Trillaud, Ultrasound elastography in liver, Diagnostic and Interventional Imaging 94 (5) (2013) 515 – 534.

[12] A. Sarvazyan, T. Hall, M. Urban, M. Fatemi, S. Aglyamov, B. Garra, An overview of elastography-an emerging branch of medical imaging, Current medical imaging reviews 7 (2011) 255–282.

[13] M. Pernot, K. Fujikura, S. D. Fung-Kee-Fung, E. E. Konofagou, Ecg-gated, mechanical and electromechanical wave imaging of cardiovascular tissues in vivo, Ultrasound in Medicine & Biology 33 (7) (2007) 1075 – 1085.

[14] E. E. Konofagou, J. Luo, D. Saluja, D. O. Cervantes, J. Coromilas, K. Fujikura, Noninvasive electromechanical wave imaging and conduction-relevant velocity estimation in vivo, Ultrasonics 50 (2) (2010) 208 – 215.

[15] J. Luo, K. Fujikura, L. S. Tyrie, M. D. Tilson, E. E. Konofagou, Pulse wave imaging of normal and aneurysmal abdominal aortas in vivo, IEEE Transactions on Medical Imaging 28 (4) (2009) 477–486.

[16] J. Bercoff, M. Tanter, M. Fink, Supersonic shear imaging: a new technique for soft tissue elasticity mapping, IEEE Transactions on Ultrasonics, Ferroelectrics, and Frequency Control 51 (4) (2004) 396–409.

[17] M. D. Horeh, A. Asif, H. Rivaz, Regularized tracking of shear-wave in ultrasound elastography, in: 2017 IEEE International Conference on Acoustics, Speech and Signal Processing (ICASSP), 2017, pp. 6264–6268.

[18] T. Gallot, S. Catheline, P. Roux, J. Brum, N. Benech, C. Negreira, Passive elastography: shear-wave tomography from physiological-noise correlation in soft tissues, IEEE Transactions on Ultrasonics, Ferroelectrics, and Frequency Control 58 (6) (2011) 1122–1126.

[19] K. Nightingale, M. S. Soo, R. Nightingale, G. Trahey, Acoustic radiation force impulse imaging: in vivo demonstration of clinical feasibility, Ultrasound in Medicine & Biology 28 (2) (2002) 227 – 235.

[20] J. Ophir, I. Cspedes, H. Ponnekanti, Y. Yazdi, X. Li, Elastography: A quantitative method for imaging the elasticity of biological tissues, Ultrasonic Imaging 13 (2) (1991) 111 – 134.

[21] P. Wells, H. Liang, Medical ultrasound: imaging of soft tissue strain and elasticity, Journal of the Royal Society Interface 8 (64) (2011) 1521–1549.

[22] G. Treece, J. Lindop, L. Chen, J. Housden, R. Prager, A. Gee, Real-time quasi-static ultrasound elastography, Interface focus 1 (4) (2011) 540–52.

[23] H. Rivaz, I. Fleming, L. Assumpcao, G. Fichtinger, U. Hamper, M. Choti, G. Hager, E. Boctor, Ablation monitoring with elastography: 2d in-vivo and 3d ex-vivo studies, in: Medical Image Computing and Computer-Assisted Intervention : MICCAI, Springer Berlin Heidelberg, 2008, pp. 458–466.

[24] H. Rivaz, P. Foroughi, I. Fleming, R. Zellars, E. Boctor, G. Hager, Tracked regularized ultrasound elastography for targeting breast radiotherapy, in: Medical image computing and computer-assisted intervention - MICCAI, Vol. 12, 2009, pp. 507–15.

[25] C. Hoerig, J. Ghaboussi, M. Fatemi, M. F. Insana, A new approach to ultrasonic elasticity imaging, in: SPIE Medical Imaging, 2016.

[26] O. A. Babaniyi, A. A. Oberai, P. E. Barbone, Recovering vector displacement estimates in quasistatic elastography using sparse relaxation of the momentum equation, Inverse Problems in Science and Engineering 25 (2015) 326–362.

[27] R. Mousavi, A. Sadeghi-Naini, G. J Czarnota, A. Samani, Towards clinical prostate ultrasound elastography using full inversion approach 41 (2014) 033501–12.

[28] R. Xia, G. Tao, A. K. Thittai, Dynamic frame pairing in real-time freehand elastography, IEEE Transactions on Ultrasonics, Ferroelectrics, and Frequency Control 61 (6) (2014) 979–985.

[29] T. J. Hall, Y. Zhu, C. S. Spalding, In vivo real-time freehand palpation imaging, Ultrasound in Medicine & Biology 29 (3) (2003) 427 – 435.

[30] E. Konofagou, J. Ophir, A new elastographic method for estimation and imaging of lateral displacements, lateral strains, corrected axial strains and poissons ratios in tissues, Ultrasound in Medicine & Biology 24 (8) (1998) 1183 – 1199.

[31] M. Mirzaei, A. Asif, H. Rivaz, Combining total variation regularization with window-based time delay estimation in ultrasound elastography, IEEE Transactions on Medical Imaging, (2019) in press.

[32] J. Jiang, T. J. Hall, A coupled subsample displacement estimation method for ultrasound-based strain elastography, Physics in Medicine & Biology 60 (21) (2015) 8347.

[33] S. Selladurai, A. K. Thittai, Strategies to obtain subpitch precision in lateral motion estimation in ultrasound elastography, IEEE Transactions on Ultrasonics, Ferroelectrics, and Frequency Control 65 (3) (2018) 448–456.

[34] E. Brusseau, A. Bernard, C. Meynier, P. Chaudet, V. Detti, G. Frin, O. Basset, A. Nguyen-Dinh, Specific ultrasound data acquisition for tissue motion and strain estimation: Initial results, Ultrasound in Medicine

& Biology 43 (12) (2017) 2904 – 2913.

[35] A. G. Hendriks, B. Hollnder, J. Menssen, A. Milkowski, H. H. Hansen, L. C. Korte, Automated 3d ultrasound elastography of the breast: A phantom validation study, Physics in medicine and biology 61 (2016) 2665–2679.

[36] C. Papadacci, E. A. Bunting, E. E. Konofagou, 3d quasi-static ultrasound elastography with plane wave in vivo, IEEE Transactions on Medical Imaging 36 (2) (2017) 357–365.

[37] E. S. Ebbini, Phase-coupled two-dimensional speckle tracking algorithm, IEEE transactions on ultrasonics, ferroelectrics, and frequency control 53 (5) (2006) 972–990.

[38] Q. He, L. Tong, L. Huang, J. Liu, Y. Chen, J. Luo, Performance optimization of lateral displacement estimation with spatial angular compounding, Ultrasonics 73 (2017) 9–21.

[39] J. Luo, E. E. Konofagou, Effects of various parameters on lateral displacement estimation in ultrasound elastography, Ultrasound in medicine & biology 35 (8) (2009) 1352–1366.

[40] X. Pan, K. Liu, J. Shao, J. Gao, L. Huang, J. Bai, J. Luo, Performance comparison of rigid and affine models for motion estimation using ultrasound radio-frequency signals, IEEE transactions on ultrasonics, ferroelectrics, and frequency control 62 (11) (2015) 1928–1943.

[41] M. Mirzaei, A. Asif, H. Rivaz, Ultrasound elastography utilizing pre-beam-formed data, in: 2019 IEEE 16th International Symposium on Biomedical Imaging (ISBI 2019), 2019, pp. 1725–1728.

[42] T. Varghese, E. Konofagou, J. Ophir, K. Alam, M. Bilgen, Direct strain estimation in elastography using spectral cross-correlation, Ultrasound in medicine & biology 26 (2000) 1525–37.

[43] R. Zahiri-Azar, S. E. Salcudean, Motion estimation in ultrasound images using time domain cross correlation with prior estimates, IEEE Transactions on Biomedical Engineering 53 (10) (2006) 1990–2000.

[44] J. Wang, Q. Huang, X. Zhang, Ultrasound elastography based on the normalized cross-correlation and the pso algorithm, in: 2017 4th International Conference on Systems and Informatics (ICSAI), 2017, pp. 1131–1135.

[45] X. Chen, M. J. Zohdy, E. SY, M. O'Donnell, Lateral speckle tracking using synthetic lateral phase, IEEE Transactions on Ultrasonics, Ferroelectrics, and Frequency Control 51 (5) (2004) 540–550.

[46] L. Yuan, P. C. Pedersen, Analytical phase-tracking-based strain estima-tion for ultrasound elasticity, IEEE Transactions on Ultrasonics, Ferroelectrics, and Frequency Control 62 (1) (2015) 185–207.

[47] P. Chaturvedi, M. F. Insana, T. J. Hall, Testing the limitations of 2-d companding for strain imaging using phantoms, IEEE Transactions on Ultrasonics, Ferroelectrics, and Frequency Control 45 (4) (1998) 1022–1031.

[48] L. Zhang, N. Snavely, B. Curless, S. M. Seitz, Spacetime faces: High-resolution capture for˜ modeling and animation, in: Data-Driven 3D Facial Animation, Springer, 2008, pp. 248–276.

[49] I. Cspedes, Y. Huang, J. Ophir, S. Spratt, Methods for estimation of sub-sample time delays of digitized echo signals, Ultrasonic Imaging 17 (2) (1995) 142–171.

[50] R. Zahiri-Azar, O. Goksel, S. E. Salcudean, Sub-sample displacement estimation from digitized ultrasound rf signals using multi-dimensional polynomial fitting of the cross-correlation function, IEEE Transactions on Ultrasonics, Ferroelectrics, and Frequency Control 57 (11) (2010) 2403–2420.

[51] M. T. Islam, A. Chaudhry, R. Righetti, A robust method to estimate the time constant of elastographic parameters, IEEE Transactions on Medical Imaging 38 (6) (2019) 1358–1370.

[52] M. Sridhar, M. F. Insana, Ultrasonic measurements of breast viscoelasticity, Medical physics 34 (12) (2007) 4757–4767.

[53] R. M. Sigrist, J. Liau, A. El Kaffas, M. C. Chammas, J. K. Willmann, Ultrasound elastography: review of techniques and clinical applications, Theranostics 7 (5) (2017) 1303.

[54] K. Nightingale, M. S. Soo, R. Nightingale, G. Trahey, Acoustic radiation force impulse imaging: in vivo demonstration of clinical feasibility, Ultrasound in medicine & biology 28 (2) (2002) 227–235.

[55] E. Turgay, S. Salcudean, R. Rohling, Identifying the mechanical properties of tissue by ultrasound strain imaging, Ultrasound in medicine & biology 32 (2) (2006) 221–235.

[56] J. Jensen, Field: A program for simulating ultrasound systems, Medical and Biological Engineering and Computing 34 (1996) 351–352.

[57] R. Righetti, J. Ophir, P. Ktonas, Axial resolution in elastography, Ultrasound in Medicine & Biology 28 (1) (2002) 101 – 113.

[58] J. Luo, E. E. Konofagou, A fast normalized cross-correlation calculation method for motion estimation, IEEE Transactions on Ultrasonics, Ferroelectrics, and Frequency Control 57 (6) (2010) 1347–1357.